Citation for the published paper:

Title:
An Impulse Response Function for Evaluation of UWB SAR Imaging

Author:
Viet Vu, Thomas Sjögren, Mats Pettersson, Hans Hellsten

Journal:
Transactions on Signal Processing

Year:
2010
Vol:
58
Issue:
7
Pagination:
3927-3932
URL/DOI to the paper:
10.1109/TSP.2010.2047503

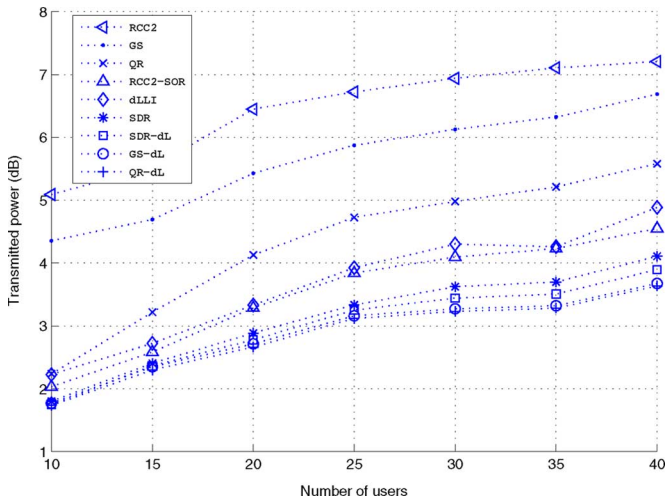

Fig. 4. Total transmitted power versus number of users; measured channel data.

There are $N = 4$ transmit antennas, and $M = 12$ user channels, measured every 3 seconds for a total of 30 temporal snapshots. In order to test with a large number of users, we randomly selected and concatenated 4 out of 30 snapshots (there are 27405 possible combinations), and averaged the results over 1000 such draws. Fig. 4 shows the transmitted power versus the number of users M. The required minimum SNR has been set to 0 dB.

It can be seen that in this figure, the QR-dL and GS-dL techniques have quite similar performance. Both of them outperform the other methods tested. These performance improvements become more significant with increasing M.

Summarizing, the results of our simulations and measured data processing clearly demonstrate an improved performance of the proposed QR-dL and GS-dL techniques with respect to the state-of-the-art multicasting methods such as the SDR, dLLI and RCC2-SOR algorithms. These improvements become especially pronounced in the large number of users case.

V. Conclusion

Two methods have been developed to approximately solve the problem of single-group multiple-antenna multicasting. The proposed techniques use channel orthogonalization and a subsequent local refinement algorithm to further improve the beamformer weight vector. Our methods have been shown via computer simulations and measured channel data processing to offer an improved performance in terms of power and spectral efficiency (and an attractive performance-to-complexity tradeoff) as compared to the current state-of-the-art multiple-antenna multicasting techniques.

Acknowledgment

The authors would like to thank the anonymous reviewers whose critical reading helped to improve the quality of this correspondence.

References

[1] N. D. Sidiropoulos, T. N. Davidson, and Z.-Q. Luo, "Transmit beamforming for physical-layer multicasting," *IEEE Trans. Signal Process.*, vol. 54, no. 6, pp. 2239–2251, Jun. 2006.

[2] M. J. Lopez, "Multiplexing, scheduling, and multicasting strategies for antenna arrays in wireless networks," Ph.D. dissertation, Electrical Eng. and Comput. Sci. Dept., MIT, Cambridge, MA, 2002.

[3] A. Lozano, "Long-term transmit beamforming for wireless multicasting," in *Proc. IEEE Int. Conf. Acoust., Speech, Signal Process. (ICASSP)*, Honolulu, HI, Apr. 2007, vol. 3, pp. 417–420.

[4] R. Hunger, D. A. Schmidt, A. S. M. Joham, and W. Utschick, "Design of single-group multicasting beamformers," in *Proc. ICC*, Glasgow, Scotland, Jun. 2007, pp. 2499–2505.

[5] E. Matskani, N. D. Sidiropoulos, Z.-Q. Luo, and L. Tassiulas, "Efficient batch and adaptive approximation algorithms for joint multicast beamforming and admission control," *IEEE Trans. Signal Process.*, vol. 57, no. 12, pp. 4882–4894, Dec. 2009.

[6] E. Matskani and N. D. Sidiropoulos, "On multicast beamforming and admission control for UMTS-LTE," in *Proc. IEEE Int. Conf. Acoust., Speech, Signal Process. (ICASSP)*, Las Vegas, NV, Apr. 2008, pp. 2361–2364.

[7] R. C. de Lamare and R. Sampaio-Neto, "Minimum mean-squared error iterative successive parallel arbitrated decision feedback detectors for DS-CDMA systems," *IEEE Trans. Commun.*, vol. 56, pp. 778–789, May 2008.

[8] E. Karipidis, N. D. Sidiropoulos, and Z.-Q. Luo, "Convex transmit beamforming for downlink multicasting to multiple co-channel groups," in *Proc. IEEE Int. Conf. Acoust., Speech, Signal Process. (ICASSP)*, Toulouse, France, May 2006.

[9] P. Goud Jr., R. Hang, D. Truhachev, and C. Schlegel, "A portable MIMO testbed and selected channel measurements," *EURASIP J. Appl. Signal Process.*, vol. 2006, manuscript ID 51490, 2006, doi:10.1155/ASP/2006/51490.

[10] N. Jindal and Z.-Q. Luo, "Capacity limits of multiple antenna multicast," in *Proc. ISIT*, Seattle, WA, Jul. 2006, pp. 1841–1845.

An Impulse Response Function for Evaluation of UWB SAR Imaging

Viet T. Vu, Thomas K. Sjögren, Mats I. Pettersson, and Hans Hellsten

***Abstract*—Based on analysis of a point target imaged by different synthetic aperture radar (SAR) systems, the commonly used impulse response function in SAR Imaging (IRF-SAR)—a two-dimensional (2-D) sinc function—is shown to be inappropriate for ultrawideband-ultrawidebeam (UWB) SAR systems utilizing a large fractional signal bandwidth and a wide antenna beamwidth. As a consequence, the applications of the 2-D sinc function such as image quality measurements and spatial resolution estimations are limited to narrowband-narrowbeam (NB) SAR systems exploiting a small fractional signal bandwidth and a narrow antenna beamwidth. In this paper, a more general IRF-SAR, which aims at UWB SAR systems, is derived with an assumption of flat two-dimensional (2-D) Fourier transform (FT) of a SAR image and called IRF-USAR. However, the derived IRF-USAR is also valid for NB SAR systems.**

***Index Terms*—Impulse response function in SAR imaging (IRF-SAR), impulse response function in UWB SAR imaging (IRF-USAR), synthetic aperture radar (SAR), Sinc, ultrawideband-ultrawidebeam (UWB).**

I. Introduction

Synthetic aperture radar (SAR) is widely used as ground-imaging radars. SAR has its own surface illuminating capability that allows it to work in hazy weather (fog, rain, etc.) and even in the night. During such unfavorable weather condition, most other remote sensing sys-

Manuscript received August 25, 2009; accepted March 21, 2010. Date of publication April 05, 2010; date of current version June 16, 2010. The associate editor coordinating the review of this manuscript and approving it for publication was Dr. Kainam Thomas Wong. This work was supported by the KK-Foundation, the Swedish Defence Research Agency, Saab Microwave Systems, and RUAG Space.

V. T. Vu, T. K. Sjögren, and M. I. Pettersson are with Blekinge Institute of Technology, Ronneby, 37225 Sweden (e-mail: viet.thuy.vu@bth.se; thomas.sjogren@bth.se; mats.pettersson@bth.se).

H. Hellsten is with Saab Microwave Systems, Gothenburg, 41289 Sweden (e-mail: hans.hellsten@saabgroup.com).

Digital Object Identifier 10.1109/TSP.2010.2047503

tems are inefficient. Ultrawideband-ultrawidebeam (UWB) SAR systems utilizing a large fractional signal bandwidth and a wide antenna beamwidth associated with very long integration time or wide integration angle enable large scene and/or high resolution imaging. The fractional bandwidth is defined by the ratio of the bandwidth to the center frequency while the integration angle by the angle between two vectors from the point target to the first and the last aperture positions. One example of experimental UWB SAR systems is CARABAS-II [1] operating in the lower VHF-band from 20 to 90 MHz and using wide beamwidth dipole antennas (larger than 90°). Other systems such as LORA operating in the VHF/UHF-bands from 200 to 800 MHz [2], P-3 with a bandwidth of 515 MHz in the VHF/UHF-bands 215–900 MHz [3], ground-based BoomSAR with a spectral response extending from 50 to 1200 MHz [4] and PAMIR with a very high bandwidth of 1820 MHz in X-band [5] are also known as UWB SAR systems. Inherent challenges in UWB SAR data processing in general and UWB SAR imaging in particular have been clearly pointed out in [6] where the choice of processing algorithm, sidelobe control or apodization, motion error compensation, and radio frequency interference (RFI) suppression are listed. Some developed approaches for such problems can be found in [7]–[10]. However, another issue, which is significantly important but has not been either mentioned or investigated in earlier publications, is the impulse response function in SAR imaging (IRF-SAR) for UWB SAR.

The commonly used IRF-SAR is known as a two-dimensional (2-D) sinc function. This function in image-domain is obtained from the 2-D Inverse Fourier Transform (IFT) of a 2-D rect function in wave-domain which is an approximation for the 2-D Fourier Transform (FT) of a SAR image of a point target. For narrowband-narrowbeam (NB) SAR systems utilizing a small fractional bandwidth and a narrow antenna beamwidth, this IRF-SAR is shown to be a good approximation. Important applications of the 2-D sinc function are found in SAR image quality measurements [11]–[13] as well as SAR spatial resolution estimations [14]–[16]. However, such the applications are limited to the NB SAR systems. For a UWB SAR system utilizing a large fractional signal bandwidth and a wide integration angle, the 2-D Fourier Transform (FT) of a SAR image of a point target is very different from the 2-D rect function. The complicated behavior of the Impulse Response in SAR imaging (IR-SAR), which refers to a SAR image of a point target, cannot therefore be represented by the 2-D sinc function in image-domain. Applying a 2-D rect function to the 2-D Fourier transform (FT) of a SAR image can result in a 2-D rect function in wave-domain and therefore a 2-D sinc function in image-domain. However, this also lead to extremely high loss in SAR spatial resolutions [10]. Such situation will therefore not be considered here. To the knowledge of the authors, there has been neither mathematical representation of IRF-SAR other than the 2-D sinc function nor investigation into the validity of the 2-D sinc function for SAR systems using large fractional signal bandwidths and wide integration angles.

The main objective of this paper is to derive a new IRF-SAR, which can be used for evaluation of UWB SAR imaging. In the context of this paper, the derived IRF-SAR is denoted by IRF-USAR, which stands for impulse response function in UWB SAR imaging. Similarly, IRF-NSAR, which stands for impulse response function in NB SAR imaging, is used for the 2-D sinc function. The IRF-USAR is derived with the assumption that the flat 2-D FT of a SAR image of a point target is flat and the derivation is limited to the monostatic case. In spite of aiming at UWB SAR systems, the derived IRF-SAR is valid for NB SAR systems.

The paper is organized as follows. Section II shows an analysis based on a point target imaged by SAR systems with various fractional bandwidths and integration angles. Motivated by the analysis in Section II, the IRF-USAR is derived in Section III. Section IV presents some basic investigations based on the derived IRF-USAR. Section V summarizes the contributions of the paper.

TABLE I
THE PARAMETERS OF THE SIMULATED SAR SYSTEMS

	System 1	System 2	System 3
Fractional bandwidth B_r	0.1	0.35	1.1
Integration angle ϕ_0	10^o	35^o	110^o

II. ANALYSIS ON POINT TARGET

In this section, we present an analysis based on a point target, which is illuminated by some SAR systems utilizing different fractional signal bandwidths and different integration angles. The main parameters of these SAR systems are summarized in Table I. The reason for this analysis is explained by the fact that the SAR system parameters decide how the point target appears in a SAR image, which directly connects to IRF-SAR. The analysis is based on simulated data to avoid undesired effects such as impacts of antenna pattern, clutter backscattering, noise and local reflection which may be caused by incompletely calibrated SAR systems. Also, no apodization technique is applied.

Image quality has a high priority in this study and it is known that both global backprojection (GBP) [17] and range migration (RM) [18] are good candidates for UWB SAR imaging in terms of quality. However, we use GBP in this study due to its advanced characteristics such as local processing and manageable motion error compensation.

In this analysis, we call sidelobes in the azimuth and range directions orthogonal sidelobes. Sidelobes in other directions, i.e. neither in the azimuth nor range directions, are called non-orthogonal sidelobes. The azimuth and range directions correspond with vertical and horizontal axes of Cartesian coordinates, respectively. In polar coordinates, they correspond with the angles of 90° and 0°, respectively.

In Fig. 1, the simulation results of a point target, which is imaged by the SAR systems in Table I, are provided. Fig. 1(a) and 1(b) shows an example of a point target imaged by a NB SAR system $h_1(x,y)$ and its 2-D FT $H_1(k_x,k_y)$, respectively. The azimuth and range are denoted by x and r while k_x and k_y indicate azimuth and range wavenumbers and are connected together by

$$\omega = \frac{c}{2}\sqrt{k_x^2 + k_y^2} \tag{1}$$

where ω is the signal frequency and c is the speed of light. The relation between a SAR image of a point target $h(x,y)$ in image-domain and its 2-D FT $H(k_x,k_y)$ in wave-domain are generally represented by

$$H(k_x,k_y) = \int_{-\infty}^{+\infty}\int_{-\infty}^{+\infty} h(x,y)\cdot \mathrm{e}^{-j(k_x x + k_y y)}dxdy. \tag{2}$$

Conversely, a SAR image of a point target $h(x,y)$ is represented by the 2-D IFT of $H(k_x,k_y)$ as

$$h(x,y) = \frac{1}{(2\pi)^2}\int_{-\infty}^{+\infty}\int_{-\infty}^{+\infty} H(k_x,k_y)\cdot \mathrm{e}^{j(k_x x + k_y y)}dk_x dk_y. \tag{3}$$

In this simulation, the NB SAR system possesses a fractional bandwidth $B_r = 0.1$ and an integration angle $\phi_0 = 10^\circ$. The 2-D FT of the SAR image $h_1(x,y)$ can be approximated by a 2-D rect function.

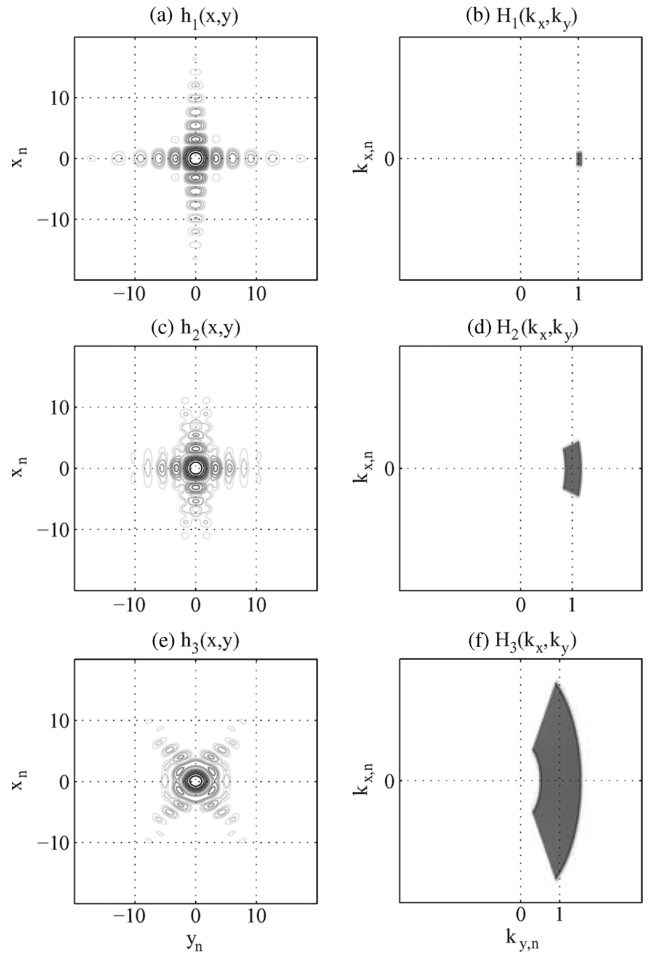

Fig. 1. Images of the point target illuminated by the different simulated SAR systems in Table I and their 2-D FT. The figures on the left-hand side (LHS) plot contours from -30 dB to -3 dB with a 3 dB step and on the right-hand side (RHS) the associated 2-D FT. The SAR image coordinates x_n and y_n denote normalized azimuth and range with respect to -3 dB widths. $k_{x,n}$ and $k_{y,n}$ denote normalized wavenumbers with respect to the center wave number k_c. (a) and (b) NB SAR with $B_r = 0.1$ and $\phi_0 = 10°$. (c) and (d) UWB SAR with $B_r = 0.35$ and $\phi_0 = 35°$. (e) and (f) UWB SAR with $B_r = 1.1$ and $\phi_0 = 110°$. (a) $\mathrm{h_1(x,y)}$. (b) $\mathrm{H_1(k_x,k_y)}$. (c) $\mathrm{h_2(x,y)}$. (d) $\mathrm{H_2(k_x,k_y)}$. (e) $\mathrm{h_3(x,y)}$. (f) $\mathrm{H_3(k_x,k_y)}$.

With the assumption of the flat 2-D FT of the SAR image, $H_1(k_x, k_y)$ of the point target imaged by the NB SAR system is given by

$$H_1(k_x, k_y) \approx \begin{cases} 1 & k_{x,\min} \le k_x \le k_{x,\max} \\ & k_{y,\min} \le k_y \le k_{y,\max} \\ 0 & \text{elsewhere.} \end{cases} \tag{4}$$

With this approximation, (3) results in a normalized SAR image in the coordinates x and y which can be mathematically represented by

$$h_1(x, y) \approx \operatorname{sinc}\left(k_c x \sin\frac{\phi_0}{2}\right) \cdot \operatorname{sinc}\left(\frac{k_{y,\max} - k_{y,\min}}{2} y\right) \tag{5}$$

where $k_{y,c}$ is the center wavenumber and ϕ_0 is the integration angle. Equation (5) is known as the IRF-NSAR. The similarity between IRF-NSAR and the SAR image given in Fig. 1(a) can be observed. The orthogonal sidelobes in the SAR image are predominated and there is no non-orthogonal sidelobe.

The investigations into the 2-D FT of the SAR image NB SAR image can also be based on models which have been proposed in [19] for the monostatic case and in [20], [21] for the bistatic case.

The point target is then illuminated by another SAR system and this time it utilizes a large fractional bandwidth $B_r = 0.35$ and an wide integration angle $\phi_0 = 35°$. As shown in Fig. 1(d), the 2-D FT of the SAR image $H_2(k_x, k_y)$ is different from a 2-D rect function. As consequence, using (5) for IRF-SAR in this case needs to be examined. The effects of fractional bandwidth and integration angle to IR-SAR can be initially observed in Fig. 1(c). The orthogonal sidelobes in the range direction start to get broader compared to Fig. 1(a). In the azimuth direction, the orthogonal sidelobes begin to attenuate and are separated into symmetric non-orthoganal sidelobes.

In the last example, we simulate the existing UWB SAR system with an extremely large fractional bandwidth $B_r = 1.1$ and an extremely wide integration angle $\phi_0 = 110°$. The 2-D FT of the SAR image $H_3(k_x, k_y)$ shown in Fig. 1(f) is clearly seen not to be a 2-D rect function. However, it can be seen as a set of one-dimensional (1-D) rect functions with the same window lengths and organized in angle of the polar coordinates. Thus, (5) cannot be used to represent the IRF-SAR for such SAR system. The point target illuminated by this UWB SAR system is plotted in Fig. 1(e) where the broadening of the range sidelobes and the strong attenuation associated with the separation of the azimuth sidelobes are observed. As a consequence of this attenuation, the orthogonal sidelobes in the azimuth direction disappear.

III. IRF-USAR

The analysis given in Section II shows that the 2-D FT of the SAR images $H(k_x, k_y)$ resulted by the SAR systems 2 and 3 in Table I should be represented by a more accurate form, which complies with the relation (1), instead of the approximate form given by (4). A flat image spectrum in wave-domain is a natural choice due to the similarities to the derivation of IRF-NSAR as well as the minimization of the -3 dB beamwidth in image-domain. Hence, a more accurate form for these SAR image spectra in the polar coordinates (κ, ϕ) can basically be given by

$$H(\kappa, \phi) = \begin{cases} 1 & -\phi_0/2 \le \phi \le \phi_0/2 \\ & \kappa_{\min} \le \kappa \le \kappa_{\max} \\ 0 & \text{elsewhere} \end{cases} \tag{6}$$

where

$$\begin{aligned} \kappa_{\min} &= k_{y,\min} \quad \text{when} \quad k_x = 0 \\ \kappa_{\max} &= k_{y,\max} \quad \text{when} \quad k_x = 0. \end{aligned} \tag{7}$$

Without losing generality, we can normalize κ with respect to the center wave-number k_c. Hence, (6) can be rewritten as

$$H(\varrho, \phi) = \begin{cases} 1 & -\phi_0/2 \le \phi \le \phi_0/2 \\ & 1 - B_r/2 \le \varrho \le 1 + B_r/2 \\ 0 & \text{elsewhere} \end{cases} \tag{8}$$

where B_r denotes the fractional bandwidth. With the approximate 2-D FT of the SAR image given in (8), the integral (3) is calculated in the polar coordinates (ϱ, ϕ) and the IRF-USAR is shown to be (see Appendix A)

$$h(\rho, \varphi, B_r, \phi_0) = \frac{\mathrm{e}^{-i\varphi}}{\rho}\left[\phi_0 \sum_{n=-\infty}^{+\infty} \frac{i^n h_{j,n-1}(\rho, B_r)}{\mathrm{e}^{i(n-1)\varphi}} \operatorname{sinc}\left(n\frac{\phi_0}{2}\right)\right] + \frac{\mathrm{e}^{-i\varphi}}{\rho} h_s(\rho, \varphi, B_r, \phi_0) \tag{9}$$

where

$$\begin{aligned} h_{j,n-1}(\rho, B_r) = &-\left(1 + \frac{B_r}{2}\right) J_{n-1}\left[\rho\left(1 + \frac{B_r}{2}\right)\right] \\ &+ \left(1 - \frac{B_r}{2}\right) J_{n-1}\left[\rho\left(1 - \frac{B_r}{2}\right)\right] \end{aligned} \tag{10}$$

and

$$h_s(\rho,\varphi,B_r,\phi_0) = -B_r \mathrm{sinc}\left[\frac{B_r}{2}\rho\cos\left(\frac{\phi_0}{2}+\varphi\right)\right] \mathrm{e}^{i\rho\cos\left(\frac{\phi_0}{2}+\varphi\right)-i\frac{\phi_0}{2}} + B_r \mathrm{sinc}\left[\frac{B_r}{2}\rho\cos\left(\frac{\phi_0}{2}-\varphi\right)\right] \times \mathrm{e}^{i\rho\cos\left(\frac{\phi_0}{2}-\varphi\right)+i\frac{\phi_0}{2}}. \quad (11)$$

In (9), the azimuth direction corresponds to $\varphi = 0^\circ$ and for the range direction $\varphi = 90^\circ$. For approximate calculation of (9), the accuracy depends strongly on the attenuation of $\mathrm{sinc}(n\phi_0/2)$. At large integration angles, this sinc function attenuates faster than at small integration angles. For example, if $\phi_0 = 110^\circ$, it is not necessary to consider the values of n beyond the range $-30 \le n \le 30$ while this range must be extended, e.g., $-300 \le n \le 300$ for $\phi_0 = 10^\circ$.

The derived IRF-USAR (9) can be simplified for particular SAR configurations. In the following example, we consider a circular aperture, i.e., $\phi_0 = 360^\circ$. Since

$$\mathrm{sinc}\left(n\frac{\phi_0}{2}\right) = \begin{cases} 1 & n = 0 \\ 0 & \text{elsewhere} \end{cases} \quad (12)$$

and

$$h_2(\rho,\varphi,B_r,\phi_0 = 360^\circ) = 0 \quad (13)$$

the derived IRF-SAR (9) is no longer a function of φ and can be rewritten as

$$h(\rho,B_r,\phi_0 = 360^\circ) = -\frac{\phi_0}{\rho}\left(1+\frac{B_r}{2}\right)J_{-1}\left[\rho\left(1+\frac{B_r}{2}\right)\right] + \frac{\phi_0}{\rho}\left(1-\frac{B_r}{2}\right)J_{-1}\left[\rho\left(1-\frac{B_r}{2}\right)\right]. \quad (14)$$

The IRF-USAR in this particular SAR configuration results in a circularly symmetric pattern which is known as a typical pattern for circular apertures [22].

IV. Evaluations of the Derived IRF-USAR

The derived IRF-USAR in Section III is first used to examine the validity of the IRF-NSAR in representing the complicated behavior of IR-SAR in both azimuth and range directions with respect to large fractional signal bandwidth and wide integration angle. In reality, IR-SAR in azimuth and range directions are normally extracted at the peak intensity belonging to the mainlobe of a single point target in a SAR image. For NB SAR systems, these IR-SAR are approximately given by the former and later sinc functions in (5). Relied on the derived IRF-USAR in Section III, the IR-SAR in azimuth and range directions are approximately found from the functions $h(\rho,90^\circ,B_r,\phi_0)$ and $h(\rho,0^\circ,B_r,\phi_0)$, respectively.

Fig. 2 plots the derived IRF-USAR associated with the SAR systems in Table I. In the plots, normalized terms are used for evaluation purposes. The intensities of IRF-USAR are normalized with respect to their peak intensity and represented in the dB scale. The horizontal axes in the plots are rescaled with respect to the -3 dB beamwidths of the sinc functions given in (5). This means, the azimuth and range are normalized with respect to the $\sin(\phi_0/2)$ and $B_r/2$, respectively. However, in these sinc functions, $k_{c,r} = 1$ and $k_{r,\max} - k_{r,\min} = B_r$ due to the normalization in the derivation of IRF-USAR. These sinc functions are also plotted in the same figures to inspect the validity

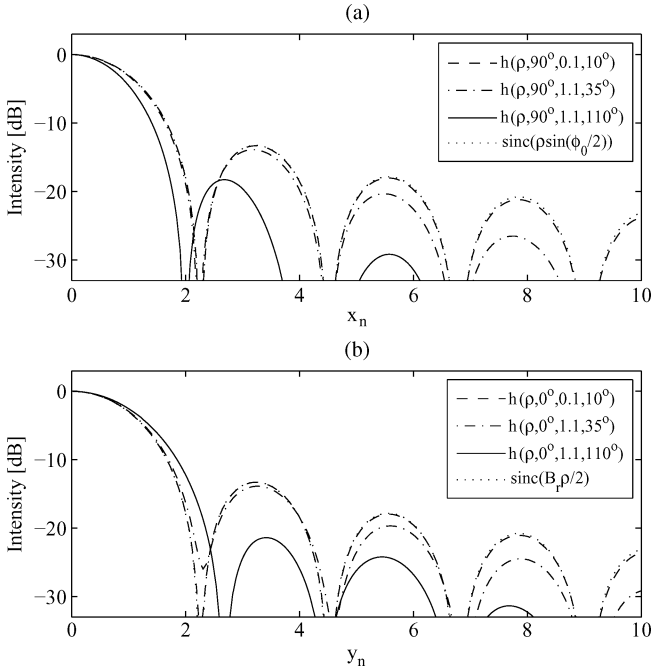

Fig. 2. Plots of $h(\rho,\varphi,B_r,\phi_0)$ with different values of the fractional bandwidths B_r and the integration angle ϕ_0 given in Table I. The intensities of IRF-USAR are normalized with respect to their peak intensity and in the dB scale. The horizontal axes in the plots are rescaled with respect to the -3 dB beamwidths of the sinc functions given in (5). The rescaled azimuth and range are denoted by x_n and y_n, respectively. The IRF-NSAR are also plotted for evaluation purposes. (a) In azimuth. (b) In range.

of IRF-NSAR for IR-SAR resulted by different SAR systems. The sinc functions and the functions $h(\rho,\varphi,0.1,10^\circ)$ are almost identical. This again confirms IRF-NSAR is a good approximation for IR-SAR resulted by NB SAR systems. This approximation may still be used for $h(\rho,\varphi,0.35,35^\circ)$. However, it does not hold for UWB SAR systems such as the SAR system 3 in Table I. In this extreme case, $h(\rho,\varphi,1.1,110^\circ)$ are considered to be significantly different from the sinc functions. These observed results are similar to the analysis results given in Section II based on SAR simulated data.

A comparison between the IR-SAR extracted at the peak intensity of the single point target in a SAR image formed by simulated data and the IR-SAR approximately generated by the derived IRF-USAR in Section III is here given to evaluate the accuracy of the IRF-USAR. Only the extreme case where $B_r = 1.1$ and $\phi_0 = 110^\circ$ is considered. Hence, the extracted IR-SAR in azimuth and range directions are given by $h_3(x,0)$ and $h_3(0,y)$, respectively, while the approximate IR-SAR are given by $h(\rho,0^0,1.1,110^\circ)$ and $h(\rho,90^0,1.1,110^\circ)$. They are plotted in Fig. 3. In the plots, we also use the normalized terms. As shown, the functions $h(\rho,\varphi,1.1,110^\circ)$ and $h_3(x,y)$ are well matched, especially the function $h(\rho,0^\circ,1.1,110^\circ)$ and $h_3(0,y)$. The observed differences in azimuth are caused by the assumption given in (8) used in the derivation. In reality, we can compensate this by an azimuth weighting function. This extreme example confirms the accuracy of the derived IRF-USAR.

We can also use the derived IRF-USAR to reconstruct the SAR image of the point target. Fig. 5 shows a three-dimensional (3-D) image of a point target reconstructed using the derived IRF-SAR where the parameters of the SAR system 3 are used and the step between values of φ is 1°. The features of the reconstructed point target are similar to the point target imaged in Fig. 1(e). The contour plots from -30 to -3 dB with a 3 dB step of this point target are

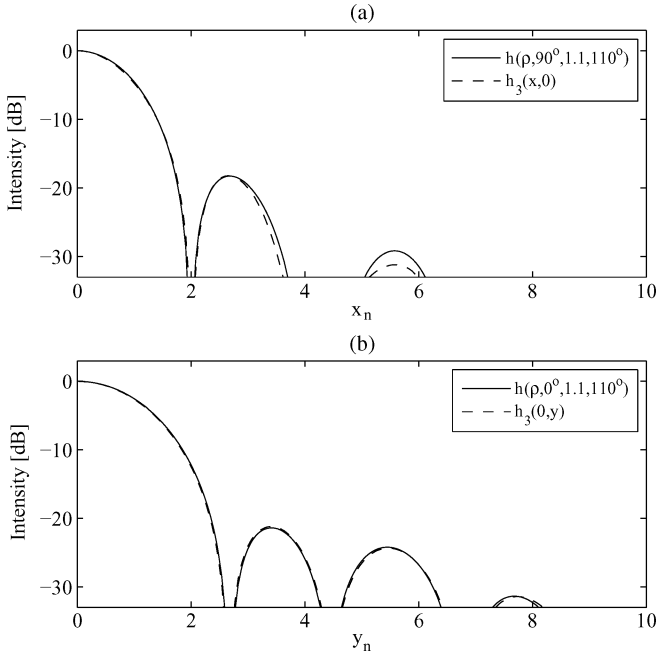

Fig. 3. Plots of IR-SAR approximately generated by $h(\rho, \varphi, 1.1, 110^\circ)$ and extracted at the peak intensity of the single point target in the SAR image given in Fig. 1(e). The intensities of IR-SAR are normalized with respect to their peak intensity and in the dB scale. The horizontal axes in the plots are also rescaled with respect to the -3 dB beamwidths of the sinc functions given in (5) and also denoted by x_n and y_n, respectively. (a) In azimuth. (b) In range.

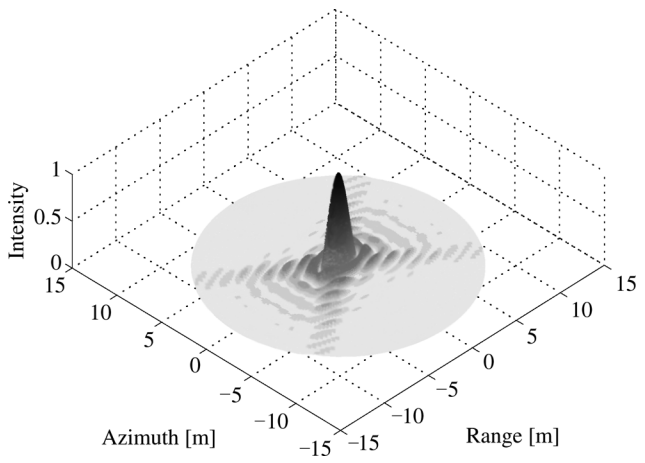

Fig. 4. The 3-D approximate SAR image of the point target is reconstructed from a set of the functions $h(\rho, \varphi, 1.1, 110^\circ)$. The intensity of the reconstructed point target is normalized with respect to its peak intensity and represented in the dimensionless scale.

also given in Fig. 4 to provide a more illustrative comparison to the contours plotted in Fig. 1(e).

Similar to the applications of the IRF-NSAR in SAR image quality measurements and spatial resolution estimations for NB SAR systems, the derived IRF-USAR also facilitates such applications for UWB SAR systems. Based on the derived function in this paper, new SAR spatial resolution equations can be developed. The methods to determine mainlobe and sidelobe areas are also supported by the new IRF-USAR. In general, UWB SAR image quality measurement procedures are simplified significantly compared to the ones given in [23]. In addition, the new IRF-USAR can be used to investigate orthogonal and nonorthogonal sidelobes resulted by UWB SAR systems and determine the limits of fractional bandwidth and integration angle to use IRF-NSAR.

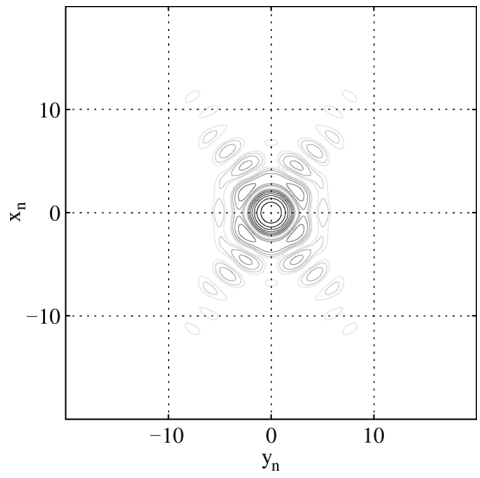

Fig. 5. Contour plots from -30 to -3 dB with a 3 dB step of the point target is reconstructed from a set of the functions $h(\rho, \varphi, 1.1, 110^\circ)$. The SAR image coordinates x_n and y_n denote normalized azimuth and range with respect to -3 dB widths.

V. Conclusion

The analysis on the point target in this paper shows that the currently used IRF-NSAR—the 2-D sinc function is mainly valid for NB SAR systems exploiting a small fractional signal bandwidth and a narrow antenna beamwidth. In reality, IRF-SAR depends strongly on these SAR system parameters. As a consequence, the applications of IRF-SAR such as image quality measurements and spatial resolution estimations are limited to NB SAR systems. This analysis is used as a basis to derive a new IRF-USAR aiming at UWB SAR systems utilizing a large fractional signal bandwidth and a wide antenna beamwidth. However, the derived IRF-USAR is also valid for NB SAR systems. The derivation is based on the assumption that the 2-D FT of a SAR image is flat. The differences between the derived IRF-USAR and IRF-NSAR are addressed in the evaluations. The accuracy of the derived function is verified by a comparison between the IR-SAR extracted at the peak intensity of the single point target in a SAR image and the approximate IR-SAR generated by the derived IRF-USAR. The derived IRF-USAR can also be used to reconstruct a SAR image of a point target. The applications of the derived IRF-USAR such as SAR image quality measurements, spatial resolution estimations, orthogonal and nonorthogonal sidelobe investigation, and examining the validity of IRF-SAR are also suggested.

Appendix A
Impulse Response Function Derivation

With a natural choice of a flat 2-D FT of a SAR image of a point target (8), the integral (3) can be normalized and transformed to polar coordinates and represented by

$$h(\rho, \varphi) = \iint \varrho \mathrm{e}^{i\varrho\rho\cos(\phi-\varphi)} d\varrho d\phi \tag{A1}$$

by simply setting

$$\begin{aligned} k_x &= \varrho \cdot \sin\phi \\ k_y &= \varrho \cdot \cos\phi \end{aligned} \tag{A2}$$

and

$$\begin{aligned} x &= \rho \cdot \sin\varphi \\ r &= \rho \cdot \cos\varphi. \end{aligned} \tag{A3}$$

The complex exponential function in the integral (A1) can be represented in terms of *Bessel* functions as [24]

$$e^{i\varrho\rho\cos(\phi-\varphi)} = \sum_{n=-\infty}^{+\infty} i^n J_n(\varrho\rho) e^{in(\phi-\varphi)}. \tag{A4}$$

Hence, the integral (A1) is rewritten as

$$h(\rho,\varphi) = \sum_{n=-\infty}^{+\infty} i^n \int \varrho J_n(\varrho\rho)d\varrho \int e^{in(\phi-\varphi)}d\phi. \tag{A5}$$

The solutions for the first and second integrals inside the summation (A5) are given by

$$\int \varrho J_n(\varrho\rho)d\varrho = \frac{1}{\rho}\left\{-\varrho J_{n-1}(\varrho\rho) + n\int J_{n-1}(\varrho\rho)d\varrho\right\} \tag{A6}$$

and

$$\int e^{in(\phi-\varphi)}d\phi = \frac{e^{in(\phi-\varphi)}}{in} \tag{A7}$$

respectively. With the limits of ϕ defined in (8), the integral (A7) results in

$$\int_{-\frac{\phi_0}{2}}^{+\frac{\phi_0}{2}} e^{in(\phi-\varphi)}d\phi = \frac{e^{in\left(\frac{\phi_0}{2}-\varphi\right)} - e^{-in\left(\frac{\phi_0}{2}+\varphi\right)}}{in}. \tag{A8}$$

The second term in (A6) and (A7) can be combined together and simplified to

$$\begin{aligned}
&\frac{1}{\rho}\int \sum_{n=-\infty}^{+\infty} i^{n-1} J_{n-1}(\varrho\rho) e^{in\left(\frac{\phi_0}{2}-\varphi\right)} d\varrho \\
&\quad - \frac{1}{\rho}\int \sum_{n=-\infty}^{+\infty} i^{n-1} J_{n-1}(\varrho\rho) e^{-in\left(\frac{\phi_0}{2}+\varphi\right)} d\varrho \\
&= \frac{e^{i\left(\frac{\phi_0}{2}-\varphi\right)}}{\rho}\int e^{i\varrho\rho\cos\left(\frac{\phi_0}{2}-\varphi\right)} d\varrho \\
&\quad - \frac{e^{-i\left(\frac{\phi_0}{2}+\varphi\right)}}{\rho}\int e^{i\varrho\rho\cos\left(\frac{\phi_0}{2}+\varphi\right)} d\varrho \\
&= \frac{e^{i\left(\frac{\phi_0}{2}-\varphi\right)} e^{i\rho\rho\cos\left(\frac{\phi_0}{2}-\varphi\right)}}{i\rho^2\cos\left(\frac{\phi_0}{2}-\varphi\right)} \\
&\quad - \frac{e^{-i\left(\frac{\phi_0}{2}+\varphi\right)} e^{i\varrho\rho\cos\left(\frac{\phi_0}{2}+\varphi\right)}}{i\rho^2\cos\left(\frac{\phi_0}{2}+\varphi\right)}.
\end{aligned} \tag{A9}$$

Substituting (A6) and (A7) to (A5) and taking (A10) into account, we get

$$\begin{aligned}
h(\rho,\varphi) = &-\phi_0 \sum_{n=-\infty}^{+\infty} \frac{i^n \varrho J_{n-1}(\varrho\rho)}{\rho e^{in\varphi}} \operatorname{sinc}\left(n\frac{\phi_0}{2}\right) \\
&\frac{+ e^{i\varrho\rho\cos\left(\frac{\phi_0}{2}-\varphi\right)+i\left(\frac{\phi_0}{2}-\varphi\right)}}{i\rho^2\cos\left(\frac{\phi_0}{2}-\varphi\right)} \\
&- \frac{e^{i\varrho\rho\cos\left(\frac{\phi_0}{2}+\varphi\right)-i\left(\frac{\phi_0}{2}+\varphi\right)}}{i\rho^2\cos\left(\frac{\phi_0}{2}+\varphi\right)}.
\end{aligned} \tag{A10}$$

The final IRF-USAR can be obtained by inserting the integral limits of ϱ given in (8).

REFERENCES

[1] H. Hellsten, L. M. H. Ulander, A. Gustavsson, and B. Larsson, "Development of VHF CARABAS II SAR," in *Proc. SPIE Radar Sens. Technol.*, Orlando, FL, Apr. 1996, vol. 2747, pp. 48–60.

[2] L. M. H. Ulander and H. Hellsten, "Airborne array aperture UWB UHF radar motivation and system considerations," *IEEE Aerosp. Electron. Syst. Mag.*, vol. 15, pp. 35–45, May 2000.

[3] D. R. Sheen, N. L. VandenBerg, S. J. Shackman, D. L. Wiseman, L. P. Elenbogen, and R. F. Rawson, "P-3 ultra-wideband SAR: Description and examples," *IEEE Aerosp. Electron. Syst. Mag.*, vol. 11, no. 11, pp. 25–30, 1996.

[4] L. Carin, N. Geng, M. McClure, J. Sichina, and L. Nguyen, "Ultra-wide-band synthetic-aperture radar for mine-field detection," *Inst. Elect. Eng. Antennas Propag. Mag.*, vol. 41, no. 1, pp. 18–33, 1999.

[5] A. R. Brenner and J. H. G. Ender, "Demonstration of advanced reconnaissance techniques with the airborne SAR/GMTI sensor PAMIR," *Inst. Elect. Eng. Proc.-Radar Sonar Navigat.*, vol. 153, no. 2, pp. 152–162, 2006.

[6] R. Goodman, S. Tummala, and W. Carrara, "Issues in ultra-wideband, widebeam SAR image formation," in *Proc. IEEE Int. Radar Conf.*, Alexandria, VA, May 1995, pp. 479–485.

[7] V. T. Vu, T. K. Sjögren, and M. I. Pettersson, "A comparison between fast factorized backprojection and frequency-domain algorithms in UWB low frequency SAR," in *Proc. IEEE IGARSS'2008*, Boston, MA, Jul. 2008, pp. 1293–1296.

[8] V. T. Vu, T. K. Sjögren, and M. I. Pettersson, "Ultrawideband chirp scaling algorithm," *IEEE Geosci. Remote Sens. Lett.*, vol. 7, no. 2, pp. 281–285, 2010.

[9] V. T. Vu, T. K. Sjögren, M. I. Pettersson, L. Håkansson, A. Gustavsson, and L. M. H. Ulander, "RFI suppression in ultra-wideband SAR using adaptive line enhancer," *IEEE Geosci. Remote Sens. Lett.*, vol. 7, no. 4, pp. 694–698, 2010.

[10] V. T. Vu, T. K. Sjögren, and M. I. Pettersson, "On apodization techniques for ultra-wideband SAR imaging," in *Proc. EURAD 2009*, Rome, Italy, Sep. 2009, pp. 529–532.

[11] M. A. and J. Marchand, "SAR image quality assessment," *Asoc. Española de Teledetección Revista de Teledetección*, vol. 2, pp. 12–18, 1993.

[12] JPL SIR-C Team, DLRNE-HF X-SAR Team, and I-PAF X-SAR Team, Data Products and Image Quality Specifications for the SIR-C/X-SAR Mission JPL Document D-7193, Mar. 1990.

[13] Envisat ASAR Cal/Val Team, Quality Measurements Definition for ASAR Level 1 Products ESA, Tech. Rep. Issue 1, Mar. 2002.

[14] W. M. Brown, "Synthetic aperture radar," *IEEE Trans. Aerosp. Electron. Syst.*, vol. AES-3, pp. 217–229, 1967.

[15] M. I. Skolnik, *Radar Handbook*, 4th ed. New York: McGraw-Hill, 1990.

[16] L. M. H. Ulander and H. Hellsten, "A new formula for SAR spatial resolution," *AEÜ Int. J. Electron. Commun.*, vol. 50, no. 2, pp. 117–121, 1996.

[17] L. E. Andersson, "On the determination of a function from spherical averages," *SIAM J. Math. Anal.*, vol. 19, no. 1, pp. 214–232, 1988.

[18] C. Cafforio, C. Prati, and F. Rocca, "SAR data focusing using seismic migration techniques," *IEEE Trans. Aerosp. Electron. Syst.*, vol. 27, pp. 194–207, Mar. 1991.

[19] R. K. Raney, "A new and fundamental Fourier transform pair," in *Proc. IEEE IGARSS'1992*, Houston, TX, May 1992, pp. 106–107.

[20] Y. L. Neo, F. H. Wong, and I. G. Cumming, "A two-dimensional spectrum for bistatic SAR processing using series reversion," *IEEE Geosci. Remote Sens. Lett.*, vol. 4, no. 1, pp. 93–96, 2007.

[21] X. Geng, H. Yan, and Y. Wang, "A two-dimensional spectrum model for general bistatic SAR," *IEEE Trans. Geosci. Remote Sens.*, vol. 46, no. 8, pp. 2216–2223, 2008.

[22] C. V. J. Jakowatz, D. E. Wahl, P. H. Eichel, D. C. Ghiglia, and P. A. Thompson, *Spotlight-Mode Synthetic Aperture Radar: A Signal Processing Approach*. Norwell, MA: Kluwer Academic, 1996, ch. 3, pp. 105–167.

[23] V. T. Vu, T. K. Sjögren, M. I. Pettersson, and A. Gustavsson, "Definition on SAR image quality measurements for UWB SAR," in *Proc. SPIE Image and Signal Process. Remote Sens. XIV*, Cardiff, U.K., Sep. 2008, vol. 7109, p. 71091A (1-9).

[24] L. Råde and B. Westergren, *Mathematics Handbook for Science and Engineering*, 4th ed. Lund, Sweden: Studentlitteratur, 1998, ch. 12, pp. 266–283.